Light transmission properties of holey metal films in the metamaterial limit: effective medium theory and subwavelength imaging

2009 New J. Phys. 11 123013

(http://iopscience.iop.org/1367-2630/11/12/123013)

New Journal of Physics
The open-access journal for physics

Light transmission properties of holey metal films in the metamaterial limit: effective medium theory and subwavelength imaging

J Jung[1,2], L Martín-Moreno[3] and F J García-Vidal[2,4]

[1] Department of Physics and Nanotechnology, Aalborg University, Skjernvej 4A, DK-9220 Aalborg Øst, Denmark
[2] Departamento de Física Teórica de la Materia Condensada, Universidad Autónoma de Madrid, E-28049 Madrid, Spain
[3] Instituto de Ciencia de Materiales de Aragón (ICMA) and Departamento de Física de la Materia Condensada, CSIC-Universidad de Zaragoza, E-50009 Zaragoza, Spain
E-mail: fj.garcia@uam.es

New Journal of Physics **11** (2009) 123013 (21pp)
Received 9 July 2009
Published 9 December 2009
Online at http://www.njp.org/
doi:10.1088/1367-2630/11/12/123013

Abstract. The light transmission properties of holey metal films in the metamaterial limit, where the unit length of the periodic structures is much smaller than the operating wavelength, are analyzed theoretically utilizing the modal expansion formalism. A detailed derivation of the transmission coefficients of both one-dimensional (1D) slit and 2D hole arrays is presented. We show that under certain assumptions the transmission coefficient becomes unity independent of the parallel momentum of the incident field. This result indicates that holey metal films can be used as endoscopes; i.e. they are capable of transforming an image with subwavelength resolution from the input to the output surface of the film. We also demonstrate how such films can effectively be mapped into homogenous anisotropic films with optical properties controlled by the geometrical parameters of the holes. Lastly, the subwavelength imaging properties of an endoscope based on a 1D slit array is demonstrated for *p*-polarized light using numerical simulations.

[4] Author to whom any correspondence should be addressed.

Contents

1. Introduction

The pioneering work of Ebbesen *et al* [1] on extraordinary optical transmission (EOT) through an optically thick metal film perforated with subwavelength holes has opened a new avenue of research within electromagnetism. This scientific avenue was at first dedicated to revealing the physics of the EOT phenomenon [2]–[4], and later to studying light transmission through various holey metal films [5]–[7] and single subwavelength holes [8]–[14].

Ebbesen and co-workers discovered that holey metal films can exhibit transmission resonances with efficiencies orders of magnitude larger than those predicted by the standard aperture theory [15], and they also pointed out that there is a link between EOT resonances and excitation of surface plasmon polaritons (SPPs) in the film. A few years later, this connection was substantiated with a theoretical explanation of the EOT phenomenon [4]. Using the multiple scattering formalism, this full three-dimensional (3D) theoretical study of EOT revealed that the enhancement of the optical transmission is due to photon tunneling through SPPs formed on the individual metal–dielectric interfaces of the film. Surprisingly, the theory also predicted that EOT through holey metal films exists even when the metal is treated as a perfect electrical conductor (PEC). In the beginning, this was considered strange because a flat PEC surface does not support SPPs. However, it was also known that corrugated PEC surfaces indeed support bound surface modes, and that the corrugations strongly compress the electromagnetic (EM) field of the surface modes in the material above the surface active medium [16, 17]. More recently, it was discovered that if a PEC structure is perforated by an array of subwavelength holes, it behaves as an effective medium where the EM waves are governed by an effective dielectric constant which is form invariant with the dielectric constant of a simple plasma ($\varepsilon = 1 - \omega_p^2/\omega^2$) [18, 19]. In the case of a holey PEC surface, the plasma frequency ω_p is not an intrinsic material property, but it is given by the cut-off frequency of the hole waveguides [18, 19]. This result has two important implications. First, as the dielectric constant is reduced to the simple plasma form, it means that a holey PEC surface can support bound surface EM modes whose properties mimic those of canonical SPPs. This is because the interface between, for example, air and a medium described by a dielectric constant of the simple plasma form fulfills the criteria for the existence of bound surface modes [20]–[22]. However, as these geometrically induced SPPs (i.e. *spoof* SPPs) have a completely different origin than canonical SPPs, spoof SPPs are supported for frequencies below ω_p and not $\omega_p/\sqrt{2}$ as with canonical

SPPs [18]. This is due to the anisotropy in the optical response of the structure. Second, as the plasma frequency is given by the cut-off frequency of the hole waveguides, which is strongly dependent on the size of the waveguide, this *plasma frequency* can be tailored by means of the size of the holes. Recently, the existence of spoof SPPs governed by the cut-off frequency of the hole waveguide has been experimentally verified in the microwave regime [23]. It is now generally accepted that EOT through holey metal films is attributable to photon tunneling through SPPs formed on the two surfaces of the film, where the SPPs can be either spoof or a mixture of spoof and canonical SPPs depending on the conductivity of the metal. Even more generally, extraordinary transmission of waves (matter and acoustic waves, for example) can be expected whenever the surface of the structure supports surface modes [24]–[26].

Another important discovery within electromagnetism that also relies on excitation of SPPs is superlensing. Less than ten years ago, Pendry proved that a planar film with a refractive index of -1 can be used as an almost perfect lens that not only cancels out the phase delay of the propagating waves, but is also capable of compensating for the exponential decay of the evanescent ones [27]. In this seminal work, Pendry showed that in the electrostatic limit where the two polarizations become decoupled, near-field superlensing can be achieved with a thin metal slab. This was later verified by experiment [28, 29]. The physical mechanism behind electrostatic superlensing is enhancement of evanescent waves by means of resonantly excited SPPs [27]. At the spectral location where the permittivity of the metal ε_{m} fulfills $-\varepsilon_{\mathrm{m}} \sim \varepsilon$, ε being the permittivity of the dielectric that surrounds the metal, the SPP dispersion relation becomes virtually flat for large parallel momenta, meaning that the band of parallel momentum where it is possible to excite SPPs becomes very broad, which results in the superlensing effect [28].

In [30], we presented a theoretical analysis of holey metal films based on the multiple scattering formalism. The original idea was to take advantage of the spoof SPP concept in holey metal films in order to transfer Pendry's idea of superlensing in the optical regime to lower frequencies. We found that spoof SPPs on holey metal films are not able to amplify the EM field associated with the incident evanescent waves as canonical SPPs do in an un-corrugated metal film. Instead, our theoretical analysis demonstrated that in the metamaterial limit ($\lambda \gg d$, where d is the unit cell size of the holey metal film), where diffraction effects can be neglected, and at some resonant Fabry–Perot frequencies, all incident plane waves (both propagating and evanescent) are transmitted with unit efficiency, meaning that a holey metal film can act as a perfect endoscope, where an image is transferred from the input surface to the output surface with a subwavelength resolution. As a difference, in the EOT regime ($\lambda \sim d$), where diffraction effects are important, spoof SPPs help to enhance the incident propagating plane waves, but their spectral location is very sensitive to the parallel momentum, i.e. angle of incidence.

Other examples of metamaterials that have been investigated for subwavelength imaging are layered metal-dielectric media [31]–[35], metallic wire media [36]–[39] and photonic crystals [40]–[43]. Some of these, e.g. metallic wire media, can also work as superlenses at terahertz frequencies, where they are capable of transforming all incoming plane waves with unit efficiency through the medium. Thus, as with holey metal films, a lens based on a metallic wire medium can transform an image with subwavelength details across the lens. However, unlike metal wire media, holey metal films are readily implemented and therefore much more attractive from an applications point of view. With the nanofabrication tools available today, it is considered an easy task to make holes in metal films, even on a scale of sub-optical wavelengths. It is also important to notice that Babinet's principle is not applicable for screens

of finite width, so there is no obvious relation between holey metal films and metallic wire media. Hence, the previous work on metallic wire media [36]–[39] cannot be used to explain the optical transmission properties of the holey metal films analyzed in this work.

This paper is a follow up to our short paper [30], where some of our work on holey metal films was presented on a superior level. In this work, we present in detail the derivation of the transmission coefficients for light transmission through holey metal films using the modal expansion formalism. We also analyze the effective optical properties of holey metal films and derive how holey metal films can be mapped into anisotropic homogenous media, with optical properties determined by the geometrical parameters of the holes in the film. Lastly, we present subwavelength imaging through an analysis of an endoscope consisting of a PEC film perforated with an arrangement of periodic cut-through 1D slits. Important issues, such as the ultimate resolution and optimal configuration of the holes, are also analyzed and discussed.

The paper is organized as follows. Section 2 is devoted to the set up and study of the transmission coefficients of holey metal films. The 1D slit and 2D hole arrays are analyzed in individual subsections (2.1 and 2.2, respectively). In section 3, the effective optical properties of holey metal films are analyzed, and section 4 presents a discussion of subwavelength imaging. In section 5, we deliver our conclusions.

2. Light transmission through holey metal films in the metamaterial limit

The transmission coefficients of holey metal films are derived using the quasi-analytical modal expansion formalism. The idea of the formalism is to expand the EM field in terms of plane wave eigenmodes outside the film and in waveguide eigenmodes inside the holes of the film. We assume that the metals of the films are PECs and that the fields in the metal regions are therefore zero. The PEC assumption is valid for low frequencies and all the way up to terahertz frequencies. We consider an incident p-polarized plane wave with parallel momentum described by k_x (thus $k_y = 0$). Inside the holes several waveguide modes will be excited by the incident field, but in the metamaterial limit only the fundamental waveguide mode will be important for the transmission properties, as all higher order modes are strongly evanescent [4]. By matching the EM fields at the input and output surfaces a self-consistent set of linear equations is obtained.

2.1. One-dimensional (1D) slit array

First we analyze an array of 1D apertures (slits) drilled into a PEC film of thickness h. The width of the slits is a and the size of the unit cell is d. We assume that the media outside the film and within the holes are the same, and described by a dielectric constant $\varepsilon = 1$. The coordinate system is chosen so that the z-axis is perpendicular to the film plane, and $z = 0$ and $z = h$ are the positions of the input and output surfaces of the film, respectively (figure 1).

We consider the case where the film is illuminated by a p-polarized plane wave, which only has parallel momentum along the x-axis ($k_\parallel = k_x$). The EM field associated with the incident field at point $\vec{r} = (x, z)$ is given as

$$\mathbf{E}_{\mathrm{i}}(\vec{r}) = \frac{1}{\sqrt{d}} \mathrm{e}^{\mathrm{i}k_x x} \mathrm{e}^{\mathrm{i}k_z z} \left(\hat{x} - \frac{k_x}{k_z} \hat{z} \right), \qquad \mathbf{H}_{\mathrm{i}}(\vec{r}) = \frac{Y}{\sqrt{d}} \mathrm{e}^{\mathrm{i}k_x x} \mathrm{e}^{\mathrm{i}k_z z} \hat{y}, \tag{1}$$

where $Y = k_0/k_z$ is the admittance, $k_z = \sqrt{k_0^2 - k_x^2}$, $k_0 = \omega/c$, ω is the angular frequency, and c is the speed of light in vacuum. The refracted and transmitted plane waves associated with

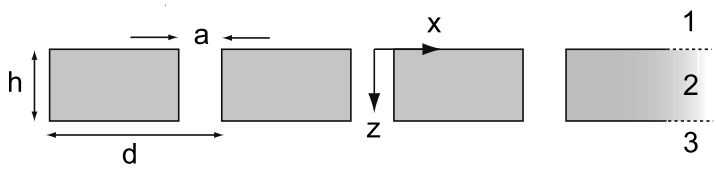

Figure 1. The 1D film perforated with subwavelength slits. The film thickness is h, the width of the slits is a and the size of the unit cell is d. The film is illuminated from region 1 by a p-polarized incident field characterized by the parallel momentum $k_{\|} = k_x$.

the nth order of diffraction can be written as

$$\mathbf{E}^{(n)}(\vec{r}) = \frac{1}{\sqrt{d}} e^{ik_x^{(n)}x} e^{\pm ik_z^{(n)}z} \left(\hat{x} - \frac{k_x^{(n)}}{k_z^{(n)}}\hat{z}\right),$$

$$\mathbf{H}^{(n)}(\vec{r}) = \frac{\pm Y^{(n)}}{\sqrt{d}} e^{ik_x^{(n)}x} e^{\pm ik_z^{(n)}z} \hat{y}, \tag{2}$$

where '+' is used for the transmitted plane waves in region 3 and '−' is used for reflected plane waves in region 1 (see figure 1), $k_x^{(n)} = k_x + n2\pi/d$, $k_z^{(n)} = \sqrt{k_0^2 - k_x^{(n)2}}$ and $Y^{(n)} = k_0/k_z^{(n)}$. The EM field associated with the fundamental TEM waveguide mode inside the slits, α, can be written as

$$\mathbf{E}_\alpha(\vec{r}) = \frac{1}{\sqrt{a}} e^{\pm ik_0 z}\hat{x}, \qquad \mathbf{H}_\alpha(\vec{r}) = \frac{\pm Y_\alpha}{\sqrt{a}} e^{\pm ik_0 z}\hat{y}, \tag{3}$$

where '−' is used in the case of backward propagating TEM waveguides modes and the admittance is $Y_\alpha = k_0/k_0 = 1$. The x component of the electric field E_x, that must be continuous at every point within the unit cell, can be expanded in terms of the eigenmodes in the three different regions (before, in, and after the film) as

$$|E_x^1\rangle = |k_x\rangle e^{ik_z z} + \sum_{n=-\infty}^{\infty} \rho^{(n)} |k_x^{(n)}\rangle e^{-ik_z^{(n)}z},$$

$$|E_x^2\rangle = |\alpha\rangle \left(A e^{ik_0 z} + B e^{-ik_0 z}\right),$$

$$|E_x^3\rangle = \sum_{n=-\infty}^{\infty} t^{(n)} |k_x^{(n)}\rangle e^{ik_z^{(n)}(z-h)}, \tag{4}$$

where we have introduced the Dirac notation as

$$\langle \mathbf{r}|k_x^{(n)}\rangle = \frac{e^{ik_x^{(n)}x}}{\sqrt{d}}, \qquad \langle \mathbf{r}|\alpha\rangle = \frac{1}{\sqrt{a}} \qquad \text{and} \qquad \langle \mathbf{r}|\vec{E}\rangle \equiv \vec{E}(\vec{r}), \tag{5}$$

and $\rho^{(n)}$ and $t^{(n)}$ are the nth order reflection and transmission coefficients, respectively, and A and B are the constants of the linear combination of the forward and backward propagating TEM waveguide modes within the holes. The magnetic field $\mathbf{H} = H_y\hat{y}$, which must be continuous only across the holes, can be related to E_x as $-\mu_z \times \mathbf{H} = \pm Y^{(n)} E_x \hat{x}$ using the

Maxwell equations, where μ_z is a unit vector along the z-direction. Thus, in the three regions

$$\begin{aligned} -\mu_z \times |\mathbf{H}^1\rangle &= Y|k_x\rangle e^{ik_z z} - \sum_{n=-\infty}^{\infty} \rho^{(n)} Y^{(n)} |k_x^{(n)}\rangle e^{-ik_z^{(n)} z}, \\ -\mu_z \times |\mathbf{H}^2\rangle &= |\alpha\rangle \left(A e^{ik_0 z} - B e^{-ik_0 z}\right), \\ -\mu_z \times |\mathbf{H}^3\rangle &= \sum_{n=-\infty}^{\infty} t^{(n)} Y^{(n)} |k_x^{(n)}\rangle e^{ik_z^{(n)}(z-h)}, \end{aligned} \tag{6}$$

must be continuous only over the holes. By matching parallel components of the electric field in equation (4) using standard boundary conditions at $z = 0$ and $z = h$ and then projecting the equations into the set $\langle k_x^{(n)}|$, one readily obtains

$$t^{(n)} = -S^{(n)} E', \qquad \rho^{(n)} = -\delta_{0,n} + S^{(n)} E, \tag{7}$$

where δ is the Kronecker delta function, $E = A + B$, $E' = -(Ae^{ik_0 h} + Be^{-ik_0 h})$ and $S^{(n)} = \langle \alpha | k_x^{(n)} \rangle$ is the overlap integral between an nth order plane wave and the TEM waveguide mode given as

$$S^{(n)} = \frac{1}{\sqrt{ad}} \int_{-a/2}^{a/2} e^{-ik_x^{(n)} x}\, dx = \sqrt{\frac{a}{d}} \operatorname{sinc}\left(\frac{k_x^{(n)} a}{2}\right). \tag{8}$$

By matching equation (6) at $z = 0$ and $z = h$, projecting the equations into the set $\langle \alpha |$, and substituting with equation (7), one obtains after some algebra a self-consistent set of linear equations in E and E'

$$\begin{aligned} (G - \Sigma)E - E' G^V &= I_0, \\ (G - \Sigma)E' - E G^V &= 0, \end{aligned} \tag{9}$$

where $I_0 = 2iY^{(0)} S^{(0)*}$, $G = i\sum_{n=-\infty}^{\infty} Y^{(n)} |S^{(n)}|^2$, $\Sigma = 1/\tan(k_0 h)$ and $G^V = 1/\sin(k_0 h)$. Solving for E' in equation (9) and substituting into equation (7) yields an expression for the transmission coefficients

$$t^{(n)} = \frac{-S^{(n)} I_0 G^V}{(G - \Sigma)^2 - G^{V2}}. \tag{10}$$

By substituting for I_0, G^V and Σ this can, after algebra, be rewritten as

$$t^{(n)} = \frac{4Y^{(0)} S^{(0)*} S^{(n)} e^{ik_0 h}}{e^{2ik_0 h}(G - i)^2 - (G + i)^2}. \tag{11}$$

In the metamaterial limit, all diffraction effects can be neglected and the transmission coefficient $t \equiv t^{(0)}$ can be reduced to

$$t = \frac{4Y^{(0)} |S^{(0)}|^2 e^{ik_0 h}}{\left[1 + Y^{(0)} |S^{(0)}|^2\right]^2 - \left[1 - Y^{(0)} |S^{(0)}|^2\right]^2 e^{2ik_0 h}}. \tag{12}$$

Equation (12) coincides with the general expression stated in [30] for the case of a 1D slit array. As a difference, in [30] the multiple scattering formalism was used in the derivation of t.

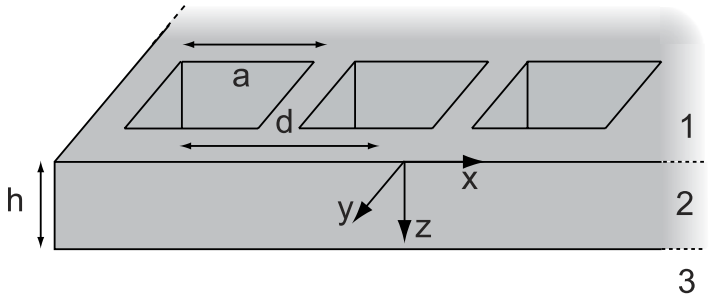

Figure 2. The 2D perfect conductor film perforated by $a \times a$ square subwavelength holes in a $d \times d$ lattice. The film thickness is h, and the film is illuminated from region 1 by a p-polarized plane wave with parallel momentum k_x.

2.2. Two-dimensional (2D) hole array

Now we consider PEC films perforated with a periodic 2D array of square holes. The hole area size is $a \times a$, the unit cell size of the lattice is $d \times d$ and the thickness of the film is h. The dielectric medium within the holes is described by the dielectric constant ε_h and the medium outside the film is described by $\varepsilon = 1$. The coordinate system is chosen so that the z-axis is perpendicular to the film plane and $z = 0$ and $z = h$ are located at the input and output surfaces of the film, respectively (figure 2). Again, we consider the case where the film is illuminated by a p-polarized plane wave ($k_\parallel = k_x$). The EM field associated with the incident field may be written as

$$\mathbf{E}_{\mathrm{i}}(\vec{r}) = \frac{1}{d}\mathrm{e}^{\mathrm{i}k_x x}\mathrm{e}^{\mathrm{i}k_z z}\left(\hat{x} - \frac{k_x}{k_z}\hat{z}\right), \qquad \mathbf{H}_{\mathrm{i}}(\vec{r}) = \frac{Y}{d}\mathrm{e}^{\mathrm{i}k_x x}\mathrm{e}^{\mathrm{i}k_z z}\hat{y}, \tag{13}$$

where $Y = k_0/k_z$ is the admittance. The EM field outside the metal film is expanded in p- and s-polarized plane wave eigenmodes. The EM field associated with an n, m order diffracted eigenmode may be expressed as

$$\begin{aligned}
\mathbf{E}_p^{(n,m)}(\vec{r}) &= \frac{1}{d}\mathrm{e}^{\mathrm{i}k_x^{(n)}x}\mathrm{e}^{\mathrm{i}k_y^{(m)}y}\mathrm{e}^{\pm\mathrm{i}k_z^{(n,m)}z}\left(\frac{k_x^{(n)}}{k_\parallel^{(n,m)}}\hat{x} + \frac{k_y^{(m)}}{k_\parallel^{(n,m)}}\hat{y} - \frac{k_\parallel^{(n,m)}}{k_z^{(n,m)}}\hat{z}\right),\\
\mathbf{E}_s^{(n,m)}(\vec{r}) &= \frac{1}{d}\mathrm{e}^{\mathrm{i}k_x^{(n)}x}\mathrm{e}^{\mathrm{i}k_y^{(m)}y}\mathrm{e}^{\pm\mathrm{i}k_z^{(n,m)}z}\left(\frac{-k_y^{(n)}}{k_\parallel^{(n,m)}}\hat{x} + \frac{k_x^{(m)}}{k_\parallel^{(n,m)}}\hat{y}\right),\\
\mathbf{H}_p^{(n,m)}(\vec{r}) &= \frac{\pm Y_p^{(n,m)}}{d}\mathrm{e}^{\mathrm{i}k_x^{(n)}x}\mathrm{e}^{\mathrm{i}k_y^{(m)}y}\mathrm{e}^{\pm\mathrm{i}k_z^{(n,m)}z}\left(\frac{-k_y^{(n)}}{k_\parallel^{(n,m)}}\hat{x} + \frac{k_x^{(m)}}{k_\parallel^{(n,m)}}\hat{y}\right),\\
\mathbf{H}_s^{(n,m)}(\vec{r}) &= \frac{\pm Y_s^{(n,m)}}{d}\mathrm{e}^{\mathrm{i}k_x^{(n)}x}\mathrm{e}^{\mathrm{i}k_y^{(m)}y}\mathrm{e}^{\pm\mathrm{i}k_z^{(n,m)}z}\left(\frac{-k_x^{(n)}}{k_\parallel^{(n,m)}}\hat{x} + \frac{-k_y^{(m)}}{k_\parallel^{(n,m)}}\hat{y} + \frac{k_\parallel^{(n,m)}}{k_z^{(n,m)}}\hat{z}\right),
\end{aligned} \tag{14}$$

where the subscripts p and s refer to p- and s-polarization, '+' is used for the transmitted eigenwaves in region 3, '−' is used for reflected eigenwaves in region 1, $k_x^{(x)} = k_x + 2\pi n/d$, $k_y^{(m)} = 2\pi m/d$, $k_z^{(n,m)} = \sqrt{k_0^2 - k_x^{(n)2} - k_y^{(m)2}}$, $k_\parallel^{(n,m)} = \sqrt{k_x^{(n)2} + k_y^{(m)2}}$ and the admittances are $Y_p^{(n,m)} = k_0/k_z^{(n,m)}$ and $Y_s^{(n,m)} = k_z^{(n,m)}/k_0$. As the EM boundary conditions only require

continuity in the parallel components (x and y) of $\mathbf{E}$ and $\mathbf{H}$, we disregard the z component and introduce bivectors in order to apply matching conditions at $z = 0$ and $z = h$. The bivectors for p and s polarization are given as

$$\begin{aligned}\langle \mathbf{r}|\mathbf{k}^{(n,m)}p\rangle &= \frac{\mathrm{e}^{\mathrm{i}k_x^{(n)}x}\,\mathrm{e}^{\mathrm{i}k_y^{(m)}y}}{dk_{\parallel}^{(n,m)}}\left(k_x^{(n)}\hat{x} + k_y^{(m)}\hat{y}\right),\\ \langle \mathbf{r}|\mathbf{k}^{(n,m)}s\rangle &= \frac{\mathrm{e}^{\mathrm{i}k_x^{(n)}x}\,\mathrm{e}^{\mathrm{i}k_y^{(m)}y}}{dk_{\parallel}^{(n,m)}}\left(-k_y^{(m)}\hat{x} + k_x^{(n)}\hat{y}\right),\end{aligned} \tag{15}$$

respectively. By means of equation (15), we can express the parallel components of the eigenmodes outside the film as

$$\begin{aligned}|\mathbf{E}_{\sigma}^{(n,m)}\rangle &= |\mathbf{k}^{(n,m)}\sigma\rangle \mathrm{e}^{\pm \mathrm{i}k_z^{(n,m)}z},\\ -\mu_z \times |\mathbf{H}_{\sigma}^{(n,m)}\rangle &= \pm Y_{\sigma}^{(n,m)}|\mathbf{k}^{(n,m)}\sigma\rangle \mathrm{e}^{\pm \mathrm{i}k_z^{(n,m)}z},\end{aligned} \tag{16}$$

where σ is the polarization (either p or s). The EM field of the fundamental TE_{01} waveguide mode within the holes α can be written as

$$\begin{aligned}\mathbf{E}_{\alpha}(\vec{r}) &= \frac{\sqrt{2}}{a}\sin\left(k_y' y + \frac{\pi}{2}\right)\mathrm{e}^{\pm \mathrm{i}k_z' z}\hat{x},\\ -\mu_z \times \mathbf{H}_{\alpha}(\vec{r}) &= \frac{\pm Y_{\alpha}\sqrt{2}}{a}\sin\left(k_y' y + \frac{\pi}{2}\right)\mathrm{e}^{\pm \mathrm{i}k_z' z}\hat{x},\end{aligned} \tag{17}$$

where '$-$' is used for backward propagating TE_{01} waveguide modes, $k_y' = \pi/a$, $k_z' = \sqrt{\varepsilon_h k_0^2 - (\pi/a)^2}$, and the admittance of the hole waveguide mode is given as $Y_{\alpha} = k_z'/k_0$. Note that primed wavevectors are used inside the holes. As in the 1D case, the parallel components of the field in the three regions (figure 2) can be expanded in terms of the eigenmodes

$$\begin{aligned}|\mathbf{E}^1\rangle &= |\mathbf{k}^{(0,0)}p\rangle \mathrm{e}^{\mathrm{i}k_z^{(0,0)}z} + \sum_{\sigma}\sum_{n,m=-\infty}^{\infty}\rho_{\sigma}^{(n,m)}|\mathbf{k}^{(n,m)}\sigma\rangle \mathrm{e}^{-\mathrm{i}k_z^{(n,m)}z},\\ |\mathbf{E}^2\rangle &= |\alpha\rangle\left[A\mathrm{e}^{\mathrm{i}k_z' z} + B\mathrm{e}^{-\mathrm{i}k_z' z}\right],\\ |\mathbf{E}^3\rangle &= \sum_{\sigma}\sum_{n,m=-\infty}^{\infty}t_{\sigma}^{(n,m)}|\mathbf{k}^{(n,m)}\sigma\rangle \mathrm{e}^{\mathrm{i}k_z^{(n,m)}(z-h)},\\ -\mu_z \times |\mathbf{H}^1\rangle &= Y_p^{(0,0)}|\mathbf{k}^{(0,0)}p\rangle \mathrm{e}^{\mathrm{i}k_z^{(0,0)}z} - \sum_{\sigma}\sum_{n,m=-\infty}^{\infty}Y_{\sigma}^{(n,m)}\rho_{\sigma}^{(n,m)}|\mathbf{k}^{(n,m)}\sigma\rangle \mathrm{e}^{-\mathrm{i}k_z^{(n,m)}z},\\ -\mu_z \times |\mathbf{H}^2\rangle &= Y_{\alpha}|\alpha\rangle\left[A\mathrm{e}^{\mathrm{i}k_z' z} - B\mathrm{e}^{-\mathrm{i}k_z' z}\right],\\ -\mu_z \times |\mathbf{H}^3\rangle &= \sum_{\sigma}\sum_{n,m=-\infty}^{\infty}t_{\sigma}^{(n,m)}Y_{\sigma}^{(n,m)}|\mathbf{k}^{(n,m)}\sigma\rangle \mathrm{e}^{\mathrm{i}k_z^{(n,m)}(z-h)}.\end{aligned} \tag{18}$$

By applying a scheme similar to the 1D case, we obtain equations for the reflection and transmission coefficients as

$$\rho_{\sigma}^{(n,m)} = -\delta_{n,0}\delta_{m,0}\delta_{\sigma,p} + S_{\sigma}^{(n,m)}E, \qquad t_{\sigma}^{(n,m)} = -S_{\sigma}^{(n,m)}E' \tag{19}$$

and a set of linear equations in $E = A + B$ and $E' = -(A\mathrm{e}^{\mathrm{i}k'_z h} + B\mathrm{e}^{-\mathrm{i}k'_z h})$, which is form invariant with equation (9). For 2D hole arrays, $I_0 = i2Y_p^{(0,0)}S_p^{(0,0)*}$, $G = \mathrm{i}\sum_\sigma \sum_{n,m=-\infty}^{\infty} Y_\sigma^{(n,m)}|S_\sigma^{(n,m)}|^2$, $\Sigma = Y_\alpha/\tan(k'_z h)$, $G^V = Y_\alpha/\sin(k'_z h)$ and $S_\sigma^{(n,m)}$ is the overlap integral between an eigenmode (of diffraction order n, m and polarization σ) and the fundamental TE_{01} waveguide mode. The overlap between the p-polarized incident field and the waveguide mode is given as

$$S_p^{(0,0)} = \frac{\sqrt{2}}{ad}\int_{-a/2}^{a/2}\int_{-a/2}^{a/2} \mathrm{e}^{\mathrm{i}k_x x}\sin\left(\frac{\pi}{a}y + \frac{\pi}{2}\right)\mathrm{d}x\,\mathrm{d}y$$
$$= \frac{2\sqrt{2}a}{d\pi}\mathrm{sinc}(k_x a/2) \tag{20}$$

and, in general, the overlap integral for p-polarization yields

$$S_p^{(n,m)} = \frac{\sqrt{2}k_x^{(n)}}{ad k_\parallel^{(n,m)}}\int_{-a/2}^{a/2}\int_{-a/2}^{a/2} \mathrm{e}^{\mathrm{i}k_x^{(n)}}\mathrm{e}^{\mathrm{i}k_y^{(m)}y}\sin\left(\frac{\pi}{a}y + \frac{\pi}{2}\right)\mathrm{d}x\,\mathrm{d}y$$
$$= \frac{-2\pi\sqrt{2}k_x^{(n)}a\,\mathrm{sinc}(k_x^{(n)}a/2)\cos(k_y^{(m)}a/2)}{dk_\parallel^{(n,m)}(k_y^{(m)}a + \pi)(k_y^{(m)}a - \pi)}. \tag{21}$$

For s-polarization, the general overlap integral can be readily found as $S_s^{(n,m)} = -k_y^{(m)}S_p^{(n,m)}/k_x^{(n)}$. By solving E' in equation (9), substituting into equation (19), and using the analytical expressions for G^V, Σ and I_0, one obtains after algebra a final result for the transmission coefficients of 2D hole arrays

$$t_\sigma^{(n,m)} = \frac{4Y_\alpha Y_p^{(0,0)}S_p^{(0,0)*}S_\sigma^{(n,m)}\mathrm{e}^{\mathrm{i}k'_z h}}{\mathrm{e}^{2\mathrm{i}k'_z h}(G - \mathrm{i}Y_\alpha)^2 - (G + \mathrm{i}Y_\alpha)^2}. \tag{22}$$

In the metamaterial limit, where all diffraction effects can be neglected, the only nonzero transmission coefficient $t \equiv t_p^{(0,0)}$ [$S \equiv S_p^{(0,0)}$ and $Y \equiv Y_p^{(0,0)}$] reduces to

$$t = \frac{4Y_\alpha Y|S|^2\mathrm{e}^{\mathrm{i}k'_z h}}{\left[Y_\alpha + Y|S|^2\right]^2 - \left[Y_\alpha - Y|S|^2\right]^2\mathrm{e}^{2\mathrm{i}k'_z h}}, \tag{23}$$

which coincides with the general expression stated in [30] for the case of a 2D hole array.

3. Effective medium theory of holey metal films in the metamaterial limit

In this section, we present a scheme for deriving the effective optical parameters of holey metal films. Using these, holey metal films can be effectively mapped into anisotropic homogenous media. The method is to set up expressions for the transmission coefficients of anisotropic homogenous films, compare them to the metamaterial limit transmission coefficients of holey metal films (equation (12) for 1D slit arrays and equation (23) for 2D hole arrays) and, from the comparison, extract the effective optical parameters of the holey metal films. We present the full scheme for 2D hole arrays. For 1D slit arrays, we only present the starting point and the final results. In the case of a 1D slit array, the starting point is that a corresponding anisotropic

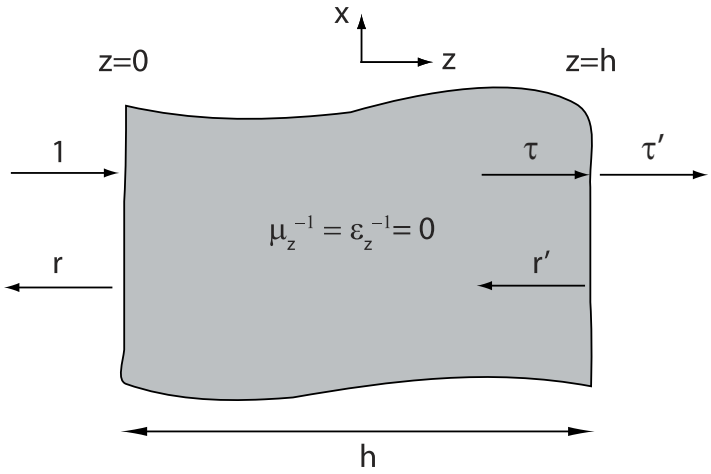

Figure 3. Light transmission through an anisotropic film of thickness h.

homogenous film would have permittivity and permeability tensors of the form [19]

$$\bar{\varepsilon}_{1D}^{-1} = \begin{bmatrix} \varepsilon_x^{-1} & 0 & 0 \\ 0 & 0 & 0 \\ 0 & 0 & 0 \end{bmatrix}, \qquad \bar{\mu}_{1D}^{-1} = \begin{bmatrix} 1 & 0 & 0 \\ 0 & \mu_y^{-1} & 0 \\ 0 & 0 & \mu_z^{-1} \end{bmatrix}. \tag{24}$$

In the case of a 2D hole array with square holes in a square lattice, symmetry requires that the response tensors have diagonal elements of the form $\varepsilon_x = \varepsilon_y = \varepsilon_\parallel$ and $\mu_x = \mu_y = \mu_\parallel$. Furthermore, as the fundamental waveguide mode within the holes shows no dispersion with the parallel momentum, a further requirement is $\varepsilon_z = \mu_z = \infty$ [18, 19]. The relative permittivity and permeability tensors of a corresponding anisotropic homogenous film therefore take the form

$$\bar{\varepsilon}_{2D}^{-1} = \begin{bmatrix} \varepsilon_\parallel^{-1} & 0 & 0 \\ 0 & \varepsilon_\parallel^{-1} & 0 \\ 0 & 0 & 0 \end{bmatrix}, \qquad \bar{\mu}_{2D}^{-1} = \begin{bmatrix} \mu_\parallel^{-1} & 0 & 0 \\ 0 & \mu_\parallel^{-1} & 0 \\ 0 & 0 & 0 \end{bmatrix}. \tag{25}$$

We now start the derivation for 2D hole arrays. The first step is to set up the transmission coefficient for light through an anisotropic homogenous film of thickness h using the response tensors of equation (25) (figure 3). We consider monochromatic plane waves, where $\nabla\times \to \mathrm{i}\mathbf{k}\times$ and $\partial/\partial t \to -\mathrm{i}\omega$. Starting from the Maxwell curl equations in $\mathbf{k}$ and ω space, the wave equation of the electric displacement $\mathbf{D}$ within the film can be written as

$$k_0^2\mathbf{D} = -\mathbf{k}'\times\bar{\mu}_{2D}^{-1}\mathbf{k}'\times\bar{\varepsilon}_{2D}^{-1}\mathbf{D} = -\varepsilon_\parallel^{-1}\mu_\parallel^{-1}\begin{bmatrix} -k_z'^2 & 0 & 0 \\ 0 & -k_z'^2 & 0 \\ k_x'k_z' & k_y'k_z' & 0 \end{bmatrix}\mathbf{D}. \tag{26}$$

Note again that primed wavevectors are used inside the film. Equation (26) has two degenerate nontrivial solutions, where for p-polarization the important one is

$$\mathbf{D} = k_x'\hat{x} + k_y'\hat{y} - \frac{k_x'^2 + k_y'^2}{k_z'}\hat{z}, \qquad \text{with} \quad k_z'^2 = k_0^2\varepsilon_\parallel\mu_\parallel. \tag{27}$$

For a p-polarized incident field, the wavevector in vacuum outside the film is given as $\mathbf{k}_i = k_x\hat{x} + k_z\hat{z}$. This leads to a solution of the wave equation of the electric displacement in vacuum as

$$\mathbf{D}_i = k_z\hat{x} - k_x\hat{z}, \qquad \text{with} \quad k_0^2 = k_x^2 + k_z^2. \tag{28}$$

The EM boundary conditions are that E_x and D_z must be continuous across the interface. Matching E_x and D_z at both $z = 0$ and $z = h$ (figure 3) yields two media transmission and reflection coefficients as

$$\tau = \frac{2\varepsilon_\parallel k_z' k_z}{(\varepsilon_\parallel k_z + k_z')k_x}, \qquad \tau' = \frac{2k_x}{\varepsilon_\parallel k_z + k_z'}, \qquad r = r' = \frac{\varepsilon_\parallel k_z - k_z'}{\varepsilon_\parallel k_z + k_z'}. \tag{29}$$

The transmission through the entire film is given by summing all the multiple scattering events, which yields

$$t = \frac{\tau\tau' \mathrm{e}^{\mathrm{i}k_z' h}}{1 - r'^2 \mathrm{e}^{2\mathrm{i}k_z' h}} = \frac{4\varepsilon_\parallel k_z' k_z \mathrm{e}^{\mathrm{i}k_z' h}}{(\varepsilon_\parallel k_z + k_z')^2 - (\varepsilon_\parallel k_z - k_z')^2 \mathrm{e}^{2\mathrm{i}k_z' h}}. \tag{30}$$

By comparing equation (30) with equation (23) (the metamaterial limit transmission coefficient of 2D hole arrays) an expression for $\varepsilon_\parallel$ can be extracted. First, we substitute for $Y = k_0/k_z$ and $Y_\alpha = k_z'/k_0$ in equation (23) and, rearranged, this yields

$$t = \frac{4\frac{k_z'^2}{|S|^2 k_0^2} k_z' k_z \mathrm{e}^{\mathrm{i}k_z' h}}{\left(\frac{k_z'^2}{|S|^2 k_0^2} k_z + k_z'\right)^2 - \left(\frac{k_z'^2}{|S|^2 k_0^2} k_z - k_z'\right)^2 \mathrm{e}^{2\mathrm{i}k_z' h}}, \tag{31}$$

which after comparison with equation (30) yields

$$\varepsilon_\parallel = \frac{k_z'^2}{|S|^2 k_0^2} = \frac{d^2\pi^2\varepsilon_h}{8a^2 \mathrm{sinc}^2(k_x a/2)} \left(1 - \frac{\pi^2 c^2}{a^2\omega^2\varepsilon_h}\right), \tag{32}$$

where equation (20), $k_z' = \sqrt{\varepsilon_h k_0^2 - (\pi/a)^2}$ and $k_0 = \omega/c$ have been used. In the metamaterial limit, where λ is large, $k_x a$ is small and $\varepsilon_\parallel$ can be approximated as

$$\varepsilon_\parallel = \frac{d^2\pi^2}{8a^2\varepsilon_h} \left(1 - \frac{\omega_\mathrm{p}^2}{\omega^2}\right), \tag{33}$$

where $\omega_\mathrm{p} = \pi c/(\sqrt{\varepsilon_h} a)$. As $k_z'^2 = k_0^2 \varepsilon_\parallel \mu_\parallel$, we immediately see from equation (32) that in the long wavelength limit [$\mathrm{sinc}(k_x a/2) \approx 1$]

$$\mu_\parallel = |S|^2 = \frac{8a^2}{d^2\pi^2}. \tag{34}$$

Equations (25), (33) and (34) present the effective EM response of a 2D holey metal film in the metamaterial limit. From equations (34) and (33) it is seen that the corresponding anisotropic homogenous film is described by a constant effective permeability and an effective permittivity on the canonical plasma form, where the cut-off frequency of the hole waveguide [$\pi c/(\sqrt{\varepsilon_h} a)$] plays the role of an effective plasma frequency. The same expressions were obtained when spoof SPPs were first predicted [18], although in that work the analysis was based on an infinite thick surface perforated with subwavelength holes and not on a film of finite thickness h.

In the 1D case, the effective optical parameters become

$$\varepsilon_x = \frac{d}{a\ \mathrm{sinc}^2(k_x a/2)} \approx \frac{d}{a}, \qquad \mu_y = \mu_z = \frac{a\ \mathrm{sinc}^2(k_x a/2)}{d} \approx \frac{a}{d}, \quad \mu_x = 1, \tag{35}$$

which together with equation (24) present the effective optical parameters of a 1D slit array in the metamaterial limit [19].

Our analysis shows how holey metal films can effectively be mapped into homogenous media with optical properties predominantly controlled by the geometrical parameters of the holes (d and a). This is important because optical material properties are normally regarded as intrinsic, related to the underlying electronic states and therefore difficult to change or control [44]. Note that the effective optical parameters, presented in equation (35), do not concur with the result presented in [44], where the authors derived an effective refractive index of the slit array, $n = d/a$. However, it is important to realize that in that work a scaling of the film thickness is also involved in the derivation of the effective optical response.

4. Subwavelength imaging using holey metal films

Now we consider subwavelength imaging using holey metal films. In [27], Pendry showed that a thin homogenous isotropic metal slab can be used as an electrostatic near-field superlens for p-polarization. By using two-media Fresnel reflection and transmission coefficients and by summing all multiple scattering events Pendry derived the transmission coefficient for p-polarization as

$$t = \frac{4\varepsilon k_z' k_z \mathrm{e}^{\mathrm{i}k_z' h}}{(\varepsilon k_z + k_z')^2 - (\varepsilon k_z - k_z')^2 \mathrm{e}^{2\mathrm{i}k_z' h}}, \tag{36}$$

where ε is the dielectric constant of the homogenous isotropic slab, $k_z' = \mathrm{i}\sqrt{k_x^2 + k_y^2 - \varepsilon\mu k_0^2}$ is the z component of the wavevector inside the slab, $k_z = \mathrm{i}\sqrt{k_x^2 + k_y^2 - k_0^2}$ is the z component of the wavevector in vacuum outside the slab, and h is the thickness of the slab [27]. In the electrostatic limit, where $k_0 \ll \sqrt{k_x^2 + k_y^2}$ the two z components of the wavevectors become identical $k_z' = k_z$ [27]. With this in mind, it is easy to see from equation (36) that the dependence of μ completely disappears for p-polarization in the electrostatic limit. If we take the limit of the SPP resonance frequency $\varepsilon = -1$, the transmission coefficient of p-polarization in the electrostatic limit simplifies as

$$t = \mathrm{e}^{-\mathrm{i}k_z h}, \qquad \forall \sqrt{k_x^2 + k_y^2}. \tag{37}$$

It is important to note that equation (37) is truly independent of the parallel momentum, which means that not only the phase of propagating waves is corrected, but also that evanescent waves are exponentially amplified across the lens. Thus, the proper alignment of the source, lens and image plane enables near-field perfect lensing where both propagating and evanescent waves contribute to the reconstruction of the image.

In the previous section, we derived the effective optical parameters of 2D hole arrays by requiring that the transmission coefficients of equations (30) and (31) be identical. By comparing these two equations with the transmission coefficient derived by Pendry (equation (36)), it can be seen that all three are form invariant. This is also the case for the

transmission coefficient of slit arrays (equation (12)), if it is properly rewritten. Thus, in the metamaterial limit, transmission coefficients of both 1D and 2D holey metal films can be rewritten so that they are form invariant with the expression that Pendry used to demonstrate near-field perfect lensing. Even though this is indeed true, it can readily be shown that perfect lensing is *not* possible utilizing holey metal films. Pendry's perfect lens relies on the fact that the z components of the wavevectors inside and outside the lens become identical for all parallel momenta. This can be achieved for a homogenous isotropic film either with a negative refractive index of $n = -1$, where perfect lensing can be realized for both polarizations, or in the electrostatic limit where k_z' becomes identical to k_z, as shown above. In the electrostatic limit, the two polarizations simply become decoupled and for p-polarization perfect lensing can be realized with only $\varepsilon = -1$. Likewise, for s-polarization electrostatic perfect lensing can be achieved with only $\mu = -1$. For holey metal films, however, the condition $k_z' = k_z$ for all parallel momenta cannot be met. Differing from homogenous isotropic films, the z component of the wavevector inside holey metal films is not a function of the parallel momentum; instead it is constant and fixed by the fundamental waveguide mode. As the z-component of the wavevector outside the film is always a strong function of the parallel momentum, we can therefore conclude that perfect lensing, as suggested by Pendry in [27] for isotropic homogenous films, cannot be realized with holey metal films.

A second difference between holey metal films and homogenous metal films is related to the difference between canonical SPPs and spoof SPPs. In the electrostatic limit, perfect lensing for a homogenous metal film is achieved at the SPP resonance frequency where $\varepsilon = -1$. The resonance frequency of spoof SPPs of holey metal films, on the other hand, is not at $\varepsilon_\parallel = -1$, but $\varepsilon_\parallel = 0$ [18]. Thus, in the limit $\varepsilon_\parallel = -1$, where the transmission coefficient would simplify to equation (37) if $k_z' = k_z$ were true for all $k_\parallel$, there are no well-defined resonantly excited spoof SPPs, and hence there is no physical mechanism behind a possible exponential enhancement of evanescent waves across the lens. This again prevents perfect lensing by means of holey metal films.

However, as k_z' is fixed by the fundamental waveguide mode (independently of the parallel momentum), another interesting phenomenon that can be used for subwavelength imaging exists in holey metal films. If the fixed k_z' fulfill the condition $k_z' h = m\pi$, the transmission coefficient of holey metal films simplifies significantly

$$t = (-1)^m \,\forall\, k_x, \tag{38}$$

which can be seen by substituting $k_z' h = m\pi$ into equation (30). $k_z' h = m\pi$ is the well-known Fabry–Perot resonance condition. Equation (38) shows that at some resonance wavelengths, a holey metal film can, for p-polarization, work as a perfect endoscope that is capable of transforming all waves independent of the parallel momentum from the input to the output side of the film. This means that holey metal films can transform an image with subwavelength details across the film. In contrast to the perfect lens where evanescent waves are amplified across the lens, holey metal films do not amplify the evanescent waves and therefore cannot cancel out the evanescent decay of evanescent waves outside the film. Previous work on wire media also discovered a resonant regime where all incoming plane waves are transmitted with unit efficiency through the structure; this regime was named the *canalization* regime [42]. For 1D slit and 2D square hole arrays, k_z' is k_0 and $\sqrt{\varepsilon_h k_0^2 - (\pi/a)^2}$, respectively. This yields

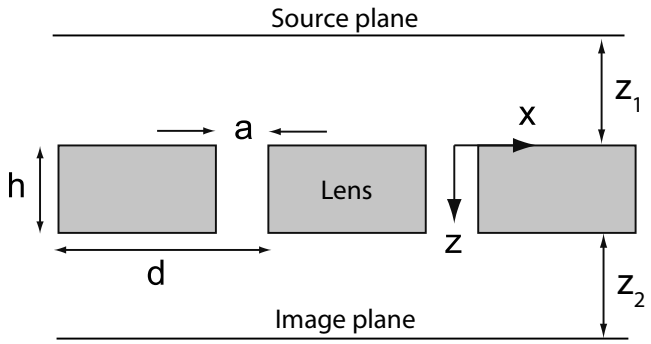

Figure 4. An incident field at a source plane at a distance z_1 from the lens is propagated through the lens and to an image plan at a distance z_2 from the lens.

resonance wavelengths for 1D slit and 2D square hole arrays as

$$\lambda_m = \frac{2h}{m}, \qquad \text{for } m \geqslant 1, \qquad \lambda_m = \frac{2\sqrt{\varepsilon_h}}{\sqrt{\left(\frac{m}{h}\right)^2 + \left(\frac{1}{a}\right)^2}}, \qquad \text{for } m \geqslant 0, \tag{39}$$

respectively. In the metamaterial limit, where $\lambda \gg d > a$, it is important to note that in order for $k_z' = \sqrt{\varepsilon_h k_0^2 - (\pi/a)^2}$ for 2D square hole arrays to be real, so that the resonance condition for subwavelength imaging ($k_z' h = m\pi$) can be fulfilled, a relatively large value of ε_h is necessary. One way to realize the resonance condition and simultaneously avoid very large values of ε_h, is to make the holes rectangular with $a_y \gg a_x$. In that case the k_z' will be $\sqrt{\varepsilon_h k_0^2 - (\pi/a_y)^2}$, which is real, even for a small ε_h, if a_y is of the order of the wavelength.

In order to prove that 1D holey metal films can work as endoscopes for p-polarization, and to support our ideas, we investigate what happens when diffraction effects are included. Using the modal expansion formalism, we present numerical calculations including all the diffraction modes needed to achieve convergence, and study in detail the imaging properties of the simplest holey metal film: a 1D slit array.

4.1. Imaging properties of slit arrays

Starting with an incident EM field at a source plane on one side of the slit array, we calculate the field at an image plane on the other side. The distance between the source plane and the slit array is denoted by z_1, and the distance between the slit array and image plane is z_2 (figure 4). We choose a p-polarized ($\mathbf{E^i} = E_x^i$) incident field that consists of two subwavelength w wide spikes separated by a subwavelength center-to-center gap distance l

$$E_x^i(x) = \begin{cases} E_0, & \text{for } \frac{-l-w}{2} < x < \frac{-l+w}{2} \text{ and } \frac{l-w}{2} < x < \frac{l+w}{2}, \\ 0, & \text{otherwise.} \end{cases} \tag{40}$$

A schematic of the incident field at the source plane can be seen in the inset of figure 5(b). Its Fourier space representation $E_x^i(k_x)$ is given as

$$E_x^i(k_x) = 2E_0 w \cos(k_x l/2)\mathrm{sinc}(k_x w/2) \tag{41}$$

Table 1. Parameters of the standard configuration of the slit array endoscope. Note that $\lambda = 2h$ is chosen as the operating wavelength. This is the first Fabry–Perot resonance with $m = 1$.

Symbol	Description	Value
a	Width of the slits	$0.5d$
h	Thickness of the slit array	$50d$
λ	Wavelength	$100d$
l	Center-to-center distance between spikes	$15d$
w	Width of the spikes	$5d$
E_0	Strength of the spikes	10
z_1	Distance between lens and image plane	0
z_2	Distance between source plane and lens	d

and the field at the image plane is calculated as

$$E_x(x) = \frac{1}{2\pi}\int_{-\infty}^{\infty} E_x^{\mathrm{i}}(k_x)E_x^{\mathrm{o}}(k_x)\mathrm{e}^{\mathrm{i}k_z z_1}\mathrm{d}k_x, \tag{42}$$

where $E_x^{\mathrm{o}}(k_x)$ is the Fourier space representation of the field at the output side of the slit array, given as a sum over all the diffracted plane waves

$$E_x^{\mathrm{o}}(k_x) = \sum_{n=-\infty}^{\infty} t^{(n)}\mathrm{e}^{\mathrm{i}k_x^{(n)}x}\mathrm{e}^{\mathrm{i}k_z^{(n)}z_2}, \tag{43}$$

where $t^{(n)}$ is the transmission coefficients specified in equation (11).

We start analysis of the slit array endoscope by introducing a configuration of parameters that specifies what we will refer to as the standard configuration of the endoscope. Investigation of how the various parameters of the endoscope affect the imaging properties of the system will be performed within the standard configuration for comparison purposes. To study subwavelength imaging, the wavelength must be larger than the parameters specifying the source $\lambda \gg w, l$, and to enter into the metamaterial limit, the unit cell size of the slit array must be smaller than the operating wavelength $\lambda \gg d$. As we are working in the PEC limit, where all results are scalable, all length parameters of the standard configuration are specified with respect to the unit length of the slit array, d. The standard parameters of the endoscope are presented in table 1. First, we will investigate the evolution of the image as the distance between the lens and the image plane z_2 is increased (figure 5). In figure 5(a), the image of the source is calculated for different z_2s, all smaller than the period of the slit array. It is seen that when z_2 is small compared to d the image of the source is distorted by the higher order diffracted waves. This is because, close to the lens, strongly evanescent higher order diffracted waves are present and will distort the perfect image that can only be obtained if all diffraction effects can be completely neglected, as they are in the derivation of equation (38). However, as the higher order diffracted waves are more strongly evanescent than the zero-order diffracted waves, they can be excluded from the image if the distance z_2 is increased. This is presented in figure 5(b), where z_2 is equal to or larger than the period of the array d. Note how the image of the subwavelength incident field is nicely reconstructed in an image with subwavelength resolution for $z_2 = d$ (blue curve).

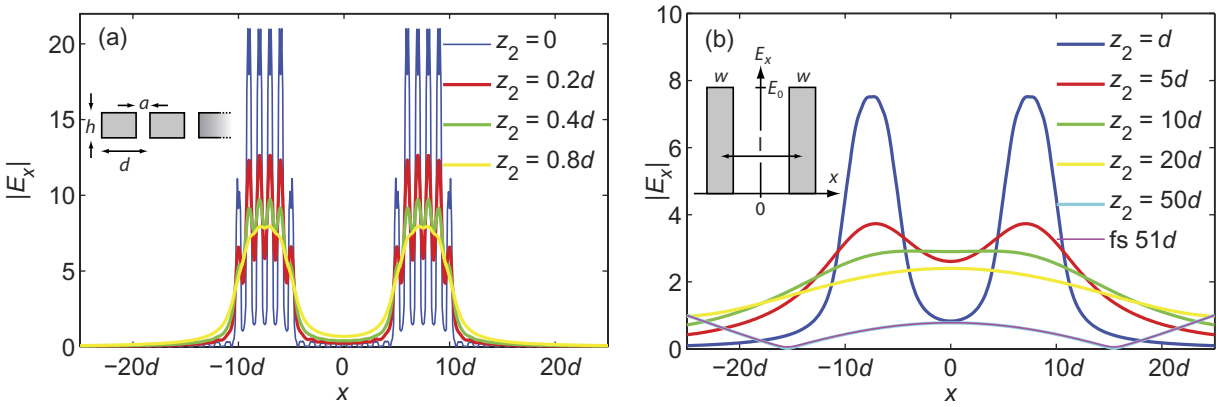

Figure 5. $|E_x(x)|$ at the image plane for different distances z_2. All other parameters are specified by the standard configuration (see table 1).

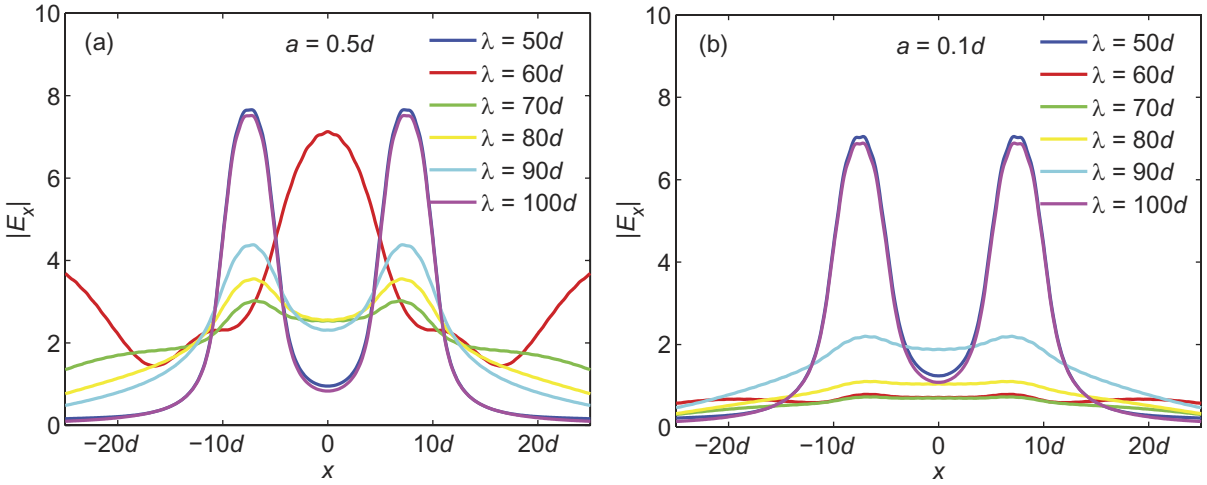

Figure 6. $|E_x(x)|$ at the image plane for different wavelengths. In (a) all other parameters are specified by the standard configuration, see table 1, and in (b) the hole size has been changed to $a = 0.1d$.

Also shown in figure 5(b) is the image after free space propagation through a distance $h + d$ (the curve with legend fs $51d$). To illustrate the effect of the slit array, this free space propagation image must be compared to the image at $z_2 = d$. It is seen that in the absence of the lens most of the source's information is lost at this plane, whereas if the lens is present a nice subwavelength image of the source is revealed. At distances $z_2 = 10d, 20d$ and $50d$ it is seen that it is no longer possible to distinguish the two spikes of the incident field. At the distance $z_2 = 50d$ the image is almost identical to the image of the free space propagation of $51d$, which indicates that the incident field is almost perfectly transmitted from the input to the output side of the slit array.

To illustrate that the endoscope effect in holey metal films is a resonant phenomenon, we next investigate how the image changes if the wavelength is varied. The image is calculated for wavelengths at and between the first- and second-order Fabry–Perot resonances ($\lambda = 2h = 100d$

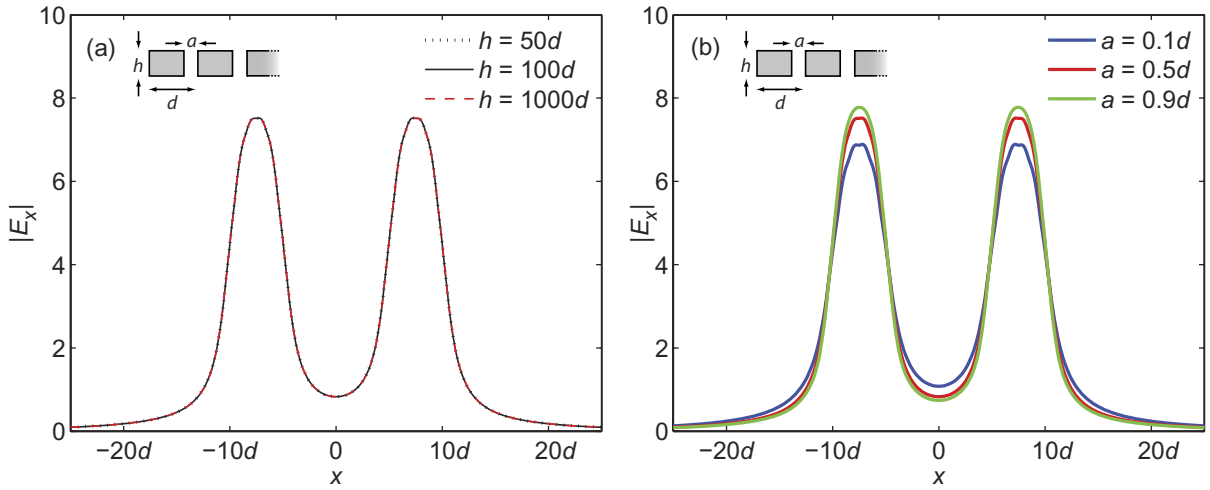

Figure 7. (a) $|E_x(x)|$ at the image plane for different thicknesses of the slit array. (b) $|E_x(x)|$ at the image plane for different hole sizes a. All other parameters are specified by the standard configuration (see table 1).

and $\lambda = h = 50d$, respectively). This is done for two hole sizes, $a = 0.5d$ in figure 6(a) and $a = 0.1d$ in figure 6(b). Both configurations show that at the two Fabry–Perot resonances almost identical images are obtained, whereas the image can be heavily distorted if the wavelength is off-resonance. For a hole size of $a = 0.5d$, the calculations show that the two Fabry–Perot resonances are approached in a different manner. For a wavelength close to the first Fabry–Perot resonance, some features of the incident field can be recognized in the image, whereas for a wavelength close to the second Fabry–Perot resonance the field is strongly oscillating and it is impossible to see features of the incident field at the image plane. By comparing the results in figures 6(a) and (b) it can be seen that the spectral bandwidth of the imaging resonances changes with the hole size of the slit array. The spectral bandwidth of the first-order imaging resonance is larger for $a = 0.5d$ than for $a = 0.1d$. This implies that larger holes are preferable in order to achieve large spectral bandwidths of the imaging resonances.

In order to show that the thickness of the slit array can be much larger than the operating wavelength, we have calculated the image for a series of thicknesses, all of them fulfilling the Fabry–Perot resonance condition $h_m = m\lambda/2 (m \geqslant 1)$ (figure 7(a)). The same result is obtained for all three thicknesses, even for the thickness h_{20}, where the slit array endoscope is 10 times thicker than the operating wavelength. This indicates that as long as the thickness of the endoscope matches the Fabry–Perot resonance condition for a given wavelength, the slit array endoscope can be of an almost arbitrary thickness.

In [30], we presented a full numerical calculation including both diffraction effects and losses, where the result showed that losses in the metal (at least in the terahertz regime) have hardly any effect on the imaging properties of the slit array endoscope. The effect of including losses in the metal was a small overall damping of the field at the image plane. Thus, even in the terahertz regime, a slit array endoscope can be made very thick and is therefore capable of transforming an image with subwavelength resolution over several wavelengths (into the far-field zone of the source). The possibility of a large z-shift of a subwavelength image is very attractive from a technological point of view, where endoscopes based on holey metal

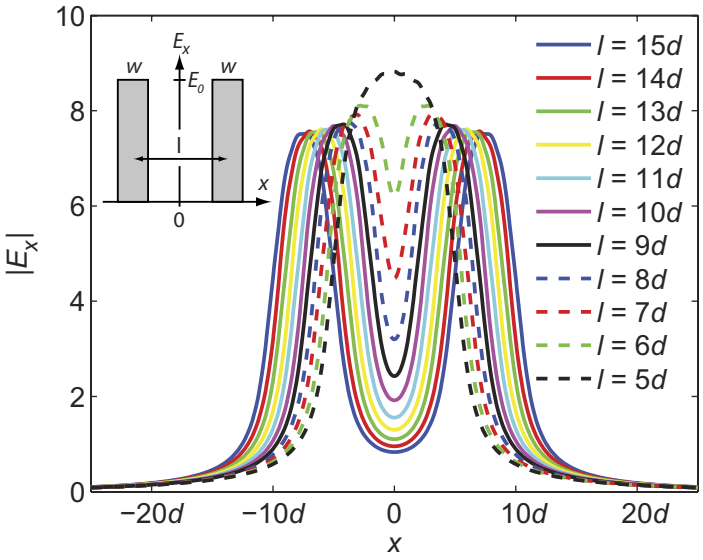

Figure 8. The gap between the spikes in the incident field is in steps reduced to zero. All other parameters are specified by the standard configuration (see table 1).

films may find many useful applications. One example could be in a scanning near-field optical microscope, where holey metal film could enable near-field optical probing in a situation where the probe is in the far-field zone of the sample.

In figure 7(b), we investigate how the image changes when we vary the width of the slits. The results show a tendency towards a slightly better image when the slits are large compared to the metal regions between them. However, the image is only marginally modified when a is varied, even if the change in a is large, as in, e.g. from $a = 0.1d$ to $a = 0.9d$ (blue and green curve, respectively).

In order to clarify how well the slit array endoscope can resolve an image, we made calculations that start from the standard configuration and reduce in steps the center-to-center distance between the two spikes of the incident field, l, until the gap between them closes (figure 8). The results show how the dip between the two spikes disappears as the two spikes approach each other. However, even for a gap size of only d (the dashed green curve for $l = 6d$) the two spikes of the source field can still be distinguished in the image. To further investigate the ultimate resolution of the slit array endoscope, we made calculations where the width of the two spikes in the incident field was varied (figure 9(a)), showing how the strength of the field is damped as the width of the two spikes is reduced. For a width of only d, the lens is still capable of producing an image where the main features of the source can still easily be recognized. In the ultimate test of the resolution of the slit array endoscope, the distance between two spikes of width d is reduced in steps to zero (figure 9(b)). Here it is seen that, even when two spikes of width d are separated by only a gap size of d, the dip in the field between the two spikes can be distinguished in the image produced by the slit array endoscope. We therefore conclude that the ultimate resolution of the slit array endoscope is in the range of the period of the slit array d. This is similar to the perfect lens in the optical regime suggested by Pendry [27], where the ultimate resolution would be the inter-atomic distance between the atoms in the lattice if absorption in the metal could be ignored [45].

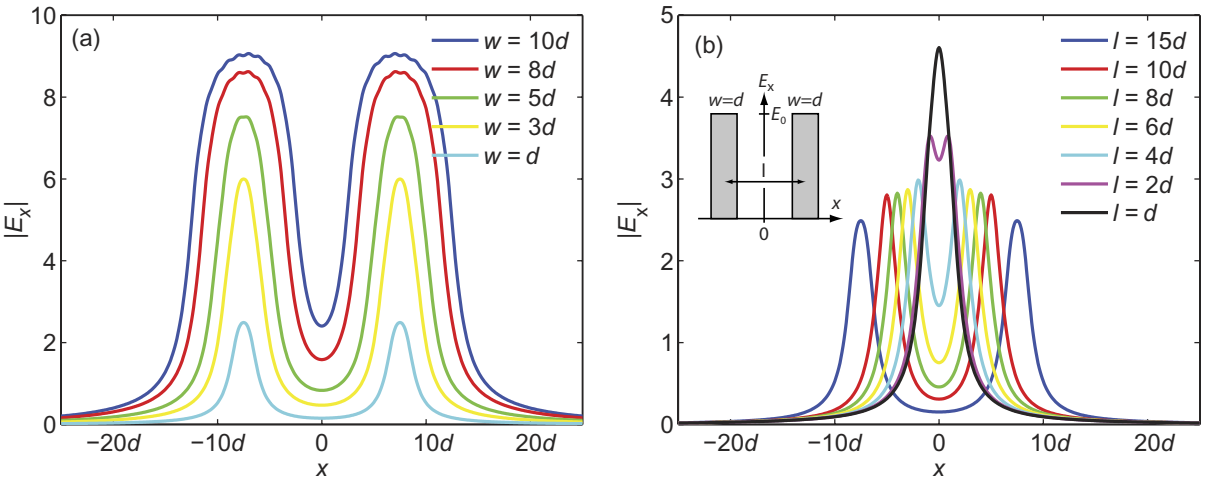

Figure 9. (a) $|E_x(x)|$ at the image plane for different widths of the spikes in the incident field. (b) The width of the spikes in the incident field is reduced to d and the gap between the spikes is reduced in steps to zero. All other parameters are specified by the standard configuration (see table 1).

5. Conclusion

Light transmission properties of holey metal films in the metamaterial limit, where the operating wavelength is much larger than the unit length of the holey metal films, have been analyzed with the focus on effective medium theory and subwavelength imaging. Transmission coefficients of both 1D slit and 2D hole arrays have been derived in the perfect conductor approximation using the modal expansion formalism. We have presented the effective medium theory of holey metal films, which shows how such films can effectively be mapped into anisotropic homogenous film with optical properties dictated by the geometrical parameters of the holes; e.g. in the case of a 2D hole array, the x and y components of the diagonal relative permittivity tensor show a Drude-like behavior, where the cut-off wavelength of the hole waveguide $\lambda = 2a\sqrt{\varepsilon_h}$ plays the role of an effective plasma frequency. We have shown that the transmission of light through holey metal films becomes particularly simple if the operating wavelength matches the Fabry–Perot resonance condition of the structure. In that case the metamaterial limit transmission coefficient for p-polarization becomes unity independent of the parallel momentum, meaning that all EM waves, both propagating and evanescent, are perfectly transmitted though the film. Using the derived modal expansion transmission coefficients, the subwavelength imaging properties of a 1D slit array endoscope have been analyzed. The analysis shows that the ultimate resolution of an endoscope, based on a 1D perfect conductor film periodically perforated with subwavelength apertures, is of the order of the unit cell size and that such an endoscope is capable of transforming an image with subwavelength resolution into the far-field zone of the source. All these properties of holey metal films make them attractive from a technological point of view and we are confident that they will find many useful applications within near-field imaging.

Acknowledgments

We thank Alexandre Mary for valuable discussions and acknowledge financial support from the Spanish Ministry of Science under project nos. CSD2007-046-NanoLight.es and MAT2008-06609-C02, and also from the Danish Research Agency through a NABIIT project (contract no. 2106-05-033).

References

[1] Ebbesen T W, Lezec H J, Ghaemi H F, Thio T and Wolff P A 1998 *Nature* **391** 667
[2] Schröter U and Heitmann D 1998 *Phys. Rev.* B **58** 15419
[3] Porto J A, Garcia-Vidal F J and Pendry J B 1999 *Phys. Rev. Lett.* **83** 2845
[4] Martin-Moreno L, Garcia-Vidal F J, Lezec H J, Pellerin K M, Thio T, Pendry J B and Ebbesen T W 2001 *Phys. Rev. Lett.* **86** 1114
[5] Bravo-Abad J, Garcia-Vidal F J and Martin-Moreno L 2004 *Phys. Rev. Lett.* **93** 227401
[6] van der Molen K L, Koerkamp K J K, Enoch S, Segerink F B, van Hulst N F and Kuipers L 2005 *Phys. Rev.* B **72** 045421
[7] Mary A, Rodrigo S G, Garcia-Vidal F J and Martin-Moreno L 2008 *Phys. Rev. Lett.* **101** 103902
[8] Grupp D E, Lezec H J, Thio T and Ebbesen T W 1999 *Adv. Mater.* **11** 860
[9] Garcia de Abajo F J 2002 *Opt. Express* **10** 1475
[10] Lezec H J, Degiron A, Devaux E, Linke R A, Martin-Moreno L, Garcia-Vidal F J and Ebbesen T W 2002 *Science* **297** 820
[11] Degiron A, Lezec H J, Yamamoto N and Ebbesen T W 2004 *Opt. Commun.* **239** 61
[12] Matteo J A, Fromm D P, Yuen Y, Schuck P J, Moerner W E and Hesselink L 2004 *Appl. Phys. Lett.* **85** 648
[13] Lockyear M J, Hibbins A P, Sambles J R and Lawrence C R 2005 *Phys. Rev. Lett.* **94** 193902
[14] Garcia-Vidal F J, Moreno E, Porto J A and Martin-Moreno L 2005 *Phys. Rev. Lett.* **95** 103901
[15] Bethe H A 1944 *Phys. Rev.* **66** 163
[16] Goubau G 1950 *J. Appl. Phys.* **21** 1119–28
[17] Mills D L and Maradudin A A 1989 *Phys. Rev.* B **39** 1569
[18] Pendry J B, Martin-Moreno L and Garcia-Vidal F J 2004 *Science* **305** 847
[19] Garcia-Vidal F J, Martin-Moreno L and Pendry J B 2005 *J. Opt. A: Pure Appl. Opt.* **7** S97
[20] Mills D L and Burstein E 1974 *Rep. Prog. Phys.* **37** 817–926
[21] Agranovich V M and Maradudin A A 1982 *Surface Polaritons—Electromagnetic Waves at Surfaces and Interfaces* 1st edn (Amsterdam: North-Holland)
[22] Novotny L and Hecht B 2006 *Principles of Nanooptics* (Cambridge: Cambridge University Press)
[23] Hibbins A P, Evans B J and Sambles J R 2005 *Science* **308** 670
[24] Moreno E, Fernandez-Dominguez A I, Cirac J I, Garcia-Vidal F J and Martin-Moreno L 2005 *Phys. Rev. Lett.* **95** 170406
[25] Christensen J, Martin-Moreno L and Garcia-Vidal F J 2008 *Phys. Rev. Lett.* **101** 014301
[26] Estrada H, Candelas P, Uris A, Belmar F, Meseguer F and de Abajo F J G 2008 *Appl. Phys. Lett.* **93** 011907
[27] Pendry J B 2000 *Phys. Rev. Lett.* **85** 3966
[28] Fang N, Lee H, Sun C and Zhang X 2005 *Science* **308** 534
[29] Melville D O S and Blaikie R J 2005 *Opt. Express* **13** 2127
[30] Jung J, Garcia-Vidal F J, Martin-Moreno L and Pendry J B 2009 *Phys. Rev.* B **79** 153407
[31] Ramakrishna S A, Pendry J B, Wiltshire M C K and Stewart W J 2003 *J. Mod. Opt.* **50** 1419
[32] Belov P A and Hao Y 2006 *Phys. Rev.* B **73** 113110
[33] Liu Z, Lee H, Xiong Y, Sun C and Zhang X 2007 *Science* **315** 1686
[34] Smolyaninov I I, Hung Y J and Davis C C 2007 *Science* **315** 1699

[35] Xiong Y, Liu Z and Zhang X 2008 *Appl. Phys. Lett.* **93** 111116
[36] Belov P A, Hao Y and Sudhakaran S 2006 *Phys. Rev.* B **73** 033108
[37] Shvets G, Trendafilov S, Pendry J B and Sarychev A 2007 *Phys. Rev. Lett.* **99** 053903
[38] Kawata S, Ono A and Verma P 2008 *Nat. Photonics* **2** 438
[39] Belov P A, Zhao Y, Tse S, Ikonen P, Silveirinha M G, Simovski C R, Tretyakov S, Hao Y and Parini C 2008 *Phys. Rev.* B **77** 193108
[40] Lou C, Johnson S G, Joannopoulos J D and Pendry J B 2002 *Phys. Rev.* B **65** 201104
[41] Parimi P V, Lu W T, Vodo P and Sridhar S 2003 *Nature* **426** 404
[42] Belov P A, Simovski C R and Ikonen P 2005 *Phys. Rev.* B **71** 193105
[43] Ikonen P, Belov P, Simovski C and Maslovski S 2006 *Phys. Rev.* B **73** 073102
[44] Shen J T, Catrysse P B and Fan S 2005 *Phys. Rev. Lett.* **94** 197401
[45] Haldane F D M 2002 arXiv:cond-mat/0206420